Materials Research Bulletin 107 (2018) 468–476

Contents lists available at ScienceDirect

Materials Research Bulletin

journal homepage: www.elsevier.com/locate/matresbu

Facile synthesis of interconnected mesoporous $ZnMn_2O_4$ nano-peanuts for Li-storage via distinct structure design

Jiajia Zou, Bing Liu*, Huanqing Liu, Yanhua Ding, Tuo Xin, Yiqian Wang*

College of Physics, Qingdao University, No. 308 Ningxia Road, Qingdao, 266071, People's Republic of China

ARTICLE INFO

Keywords:
Mesoporous
Inter-connected structure
$ZnMn_2O_4$ nano-peanuts
Lithium storage

ABSTRACT

The $ZnMn_2O_4$ nano-peanuts with diameters of 16–25 nm have been successfully prepared through a simple one-step surfactant-assisted solvothermal process. The as-synthesized $ZnMn_2O_4$ exhibits novel interconnected mesoporous hierarchical architecture, which possesses three advantages: special mesoporous structure, high specific surface and interconnected walls. On one hand, the interconnected structure can provide sufficient surface reaction sites to fully contact Li^+ with the electrolyte and improve Li^+ diffusion and electron transfer; On the other hand, the mesoporous hierarchical networks can buffer the volume change, accommodate or alleviate the strain during charge-discharge process, thus enhancing the conductivity and stability of the electrodes. Benefiting from the mesoporous design, the interconnected $ZnMn_2O_4$ delivers a stable capacity (812 mA h g^{-1} at 100 mA g^{-1} after 200 cycles), and maintains a high capacity of 516 mA h g^{-1} even at 2 A g^{-1} after 200 cycles, which shows that the nanostructured $ZnMn_2O_4$ has excellent cycling stability.

1. Introduction

Owing to the fact that traditional energy brings serious environmental pollution, the demand for clean energy is constantly increasing. Lithium-ion batteries (LIBs) have attracted tremendous attention due to their high energy density, high power density and long cycle life [1–3]. At present, graphite-based materials have been utilized as anode materials for commercial LIBs. Unfortunately, the relatively low theoretical capacity of 372 mA h g^{-1} has hindered the further application of LIBs in power vehicles and high-performance requirements [4,5]. As a consequence, it is imperative for researchers to develop novel electrode materials, especially anode materials [2,3,5]. Over the past two decades, transition metal oxides have been identified as potential candidates for high theoretical capacities, environmental friendliness and low cost. Recent studies have found that mixed transition metal oxides (MTMOs) are diverse and complementary compared with single transition metal oxides (STMOs), and thus have enhanced electrochemical performance [6–9]. Spinel-structured $ZnMn_2O_4$ with a bivalent Zn^{2+} ion at tetrahedral sites and a trivalent Mn^{3+} ion at octahedral sites stands out among the intriguing mixed manganite oxides, by the virtues of high theoretical capacity, environmental friendliness, low cost and the low oxidation potentials (i.e., delithiation potential) of zinc and manganese at 1.2 and 1.5 V (vs. Li /Li^+) [8–14], which allow large output voltage in batteries, finally resulting in a high specific energy density.

However, similar to most of high capacity materials, $ZnMn_2O_4$ suffers particle aggregation and large volume variation during charge-discharge process, which inevitably leads to polarization of electrode and a loss of inter-particle electronic contact and consequently poor stability against cycling [15–17]. $ZnMn_2O_4$ nanoparticles of 30–60 nm in size show a reversible capacity up to 569 mA h g^{-1} at a current density of 100 mA g^{-1} after 50 cycles, which may suffer particle aggregation after cycles [18]. Yuan et al. reported $ZnMn_2O_4$ hollow metal glycolate microspheres with a discharge capacity of 750 mA h g^{-1} at 400 mA g^{-1}, which may cause large volume changes and fast drop after 120 cycles [18–22]. The researchers tried their best to maintain the volume and cycling stability of $ZnMn_2O_4$, but still have no satisfactory results in the case of large volume variation and rapid drop in capacity. To solve these problems, one of the strategies is to combine with carbon material, but it will decrease the total capacity of the electrode due to the presence of low-capacity carbon. Another strategy is to design the microstructure and regulation of nanomaterials (such as porous structure), that is, to optimize electrode structure considering the stability of the electrodes.

Porous nanostructured materials can not only facilitate the transport kinetics for Li^+ and electron, but also increase the active sites of electrochemical reactions, and at the same time, they also could provide enough space to buffer volume change and avoid particle aggregation

* Corresponding authors.
E-mail addresses: bing_liu@qdu.edu.cn (B. Liu), yqwang@qdu.edu.cn (Y. Wang).

https://doi.org/10.1016/j.materresbull.2018.08.019
Received 30 May 2018; Received in revised form 31 July 2018; Accepted 12 August 2018
Available online 13 August 2018

during the discharge-charge process [15,23]. Therefore, the combination of nanocrystallization and porosity is one of the practical methods to improve the relevant electrochemical performance of electrode materials. Herein, we report the uniform mesoporous $ZnMn_2O_4$ nano-peanuts with diameters of 16–25 nm. The $ZnMn_2O_4$ nano-peanuts are not only non-toxic and environment-friendly, but also have three advantages: special mesoporous structure, high specific surface area and interconnected walls. When evaluated for LIBs, $ZnMn_2O_4$ nano-peanuts deliver a stable capacity of 812 mA h g^{-1} at 100 mA g^{-1} after 200 cycles, showing higher reversible capacity and superior cycle performance compared with bulk ZnO and bulk Mn_2O_3.

2. Experimental

All chemicals were of analytical grade and used directly without further purification. Distilled water was used throughout the whole experiments.

2.1. Synthesis of mesoporous $ZnMn_2O_4$ nano-peanuts

$ZnMn_2O_4$ nano-peanuts were synthesized by a simple solvothermal method. Firstly, 2.0 *g* of hexadecyl trimethyl ammonium bromide (CTAB) was dissolved in 50 mL ethylene glycol to form a homogeneous solution under vigorous stirring at room temperature. Secondly, 1.0 mmol of zinc acetylacetonate $Zn(acac)_2$ was added to the above solution. Thirdly, 1.0 mmol of manganese acetylacetonate $Mn(acac)_2$ was added to the former solution and then kept ultrasonically for 30 min. After that, the mixed solution was under vigorous stirring for 15 min. The obtained mixed solution was transferred into a 100 mL Teflon-sealed autoclave and maintained at 180 °C for 13 h to obtain the precursor. After the reaction system dropped to room temperature, the resultant precipitates were collected by centrifugation, washed several times with distilled water and ethanol, and then dried at 60 °C for 6 h. To obtain the uniform nano-peanuts, the precursor was annealed in air at 600 °C for 3 h at the ramp rate of 4 °C min^{-1}.

2.2. Synthesis of bulk ZnO and bulk Mn_2O_3

2.0 *g* of CTAB was dissolved in 50 mL ethylene glycol to form a homogeneous solution under vigorous stirring at room temperature and 1.0 mmol $Zn(acac)_2$ was added to the above solution. Then, the solution was sonicated for 30 min. After that, the mixture solution was vigorously stirred for 15 min. The solution was transferred into a 100 mL Teflon-sealed autoclave and maintained at 180 °C for 13 h. The resultant precipitates were collected by centrifugation and washed several times with distilled water and ethanol, and then the precipitates were dried at 60 °C for 6 h. Finally, the product was annealed in air at 600 °C for 3 h with a rate of 4 °C min^{-1}. The bulk Mn_2O_3 was synthesized under the same conditions except that $Zn(acac)_2$ was replaced by $Mn(acac)_2$.

2.3. Material characterization

Crystallographic phases of the samples were analyzed by SmartLab XRD with Cu-Kα_1 radiation (λ = 1.5406 Å). Thermogravimetric analysis (TGA) was conducted on a Netzsch TG 209 apparatus with a heating rate of 10 °C min^{-1}. X-ray photoelectron spectroscopy (XPS) was performed on a Thermo Scientific ESCALAB 250Xi instrument with monochromatic Al Kα radiation ($h\nu$ = 1486.6 eV) at ultrahigh vacuum (below 10^{-8} Pa). The binding energies were calibrated using C 1 s peak (284.8 eV) as a reference.

The morphologies and compositions of the products were observed by scanning electron microscope (SEM, Hitachi S-4800), field-emission scanning electron microscope (FESEM; Hitachi S-4800 15 kV), and energy-dispersive X-ray spectrometer (EDS Hitachi S-4800). Bright-field (BF) images and high-resolution transmission electron microscopy (HRTEM) images were obtained on a JEOL JEM2100 transmission electron microscope (TEM) with an accelerating voltage of 200 kV. The nitrogen adsorption-desorption was performed on an automatic volumetric sorption analyzer (NOVA 1100, Quantachrome, USA) at 77 K. The Brunauer-Emmett-Teller (BET) was used to calculate the specific surface areas of $ZnMn_2O_4$ nano-peanuts. The pore size distributions were obtained using Barrerr-Joyner-Halenda (BJH) method.

2.4. Electrochemical measurements

Working electrodes were prepared by mixing the as-prepared active materials ($ZnMn_2O_4$ nano-peanuts, bulk ZnO and bulk Mn_2O_3) with water-soluble sodium alginate (SA) and carbon black in a weight ratio of 70:15:15 (wt.%) on a clean copper foil. The copper was dried at 120 °C for 12 h in a vacuum oven and the CR2025-type coin cells (20 mm in diameter and 2.5 mm in thickness) were assembled in a glove box filled with argon with a moisture and oxygen concentration of less than 1 ppm. The mass loadings of $ZnMn_2O_4$, ZnO and Mn_2O_3 composites for cell testing were 1.2 mg, 1.1 mg and 1.0 mg, respectively. The electrolyte consisted of 1 M $LiPF_6$ solution of ethylene carbonate (EC)/dimethyl carbonate (DMC)/diethyl carbonate (DEC) (1:1:1 in volume). The electrochemical performances were tested on a LAND CT2001 battery test system in a voltage range of 0.01 V–3.00 V at room temperature. Cyclic voltammetry (CV) measurements (over the potential range of 0.01 V–3.00 V at a scan rate of 0.1 mV s^{-1}) and electrochemical impedance spectroscopy (EIS) tests were carried out on a Metrohm Autolab electrochemical workstation (PGSTAT 302 N) with a frequency range from 100 kHz to 0.01 Hz.

3. Results and discussion

The Zn-Mn oxides were prepared by a simple solvothermal method and carbonization process. Fig. 1a shows the XRD patterns of the products before and after annealing at 600 °C for 3 h in air. The diffraction peaks at around 33°, 36° and 38° are the characteristics of metal glycolates [24]. For the products after annealing, these peaks can be indexed to tetragonal $ZnMn_2O_4$ (JCPDS no.: 77-0470, a = b = 5.720 Å, c = 9.240 Å). The sharp diffraction peaks at 2θ of 18.22°, 29.32°, 31.24°, 33.00°, 36.41° and 60.82° can be assigned to (101), (112), (200), (103), (211) and (224) crystal planes, respectively, indicating the high purity of synthesized sample. For the ZnO and Mn_2O_3 (Fig. 1b), all the diffraction peaks correspond to hexagonal ZnO (JCPDS no.: 76-0704) and cubic Mn_2O_3 (JCPDS no.: 71-0636), respectively. Fig. 1c shows the TG-DTA analysis of the products before annealing. The TG-DTA analysis was performed in air at a ramp rate of 10 °C min^{-1} from 30 °C to 800 °C. It can be seen that there is a significant weight loss at 85–550 °C, indicating a total weight loss of 13%. The weight loss may be ascribed to the evaporation of water and the decomposition of CTAB. Subsequently, the TG curve has no significant weight loss above 550 °C, indicating that the $ZnMn_2O_4$ has excellent thermal stability at even higher temperatures. Therefore, we determine that the heat treatment temperature of the products is 600 °C, and we believe that under this condition, the precursor can be completely converted to the final $ZnMn_2O_4$.

To determine the chemical composition and chemical valence state of the as-synthesized products, XPS analysis was performed, and the results are shown in Fig. 2. Fig. 2a demonstrates the photoelectron spectra of the Zn, Mn, O and C elements, where C is inferred from the carbonate species of the XPS instrument. As shown in Fig. 2b, the peaks at 1044.4 eV and 1021.1 eV can be assigned to Zn $2p_{1/2}$ and Zn $2p_{3/2}$. The splitting gap between these two peaks is 23.3 eV, which is consistent with that of $ZnMn_2O_4$ [25]. Additionally, in Fig. 2c, The peaks at 653.9 eV and 642.1 eV can be assigned to Mn $2p_{1/2}$ and Mn $2p_{3/2}$ [26]. The energy difference between Mn $2p_{1/2}$ and Mn $2p_{3/2}$ is approximately 11.9 eV. As reported previously, it can be demonstrated that the manganese ion in the $ZnMn_2O_4$ is trivalent [27]. The O 1*s* spectrum can be

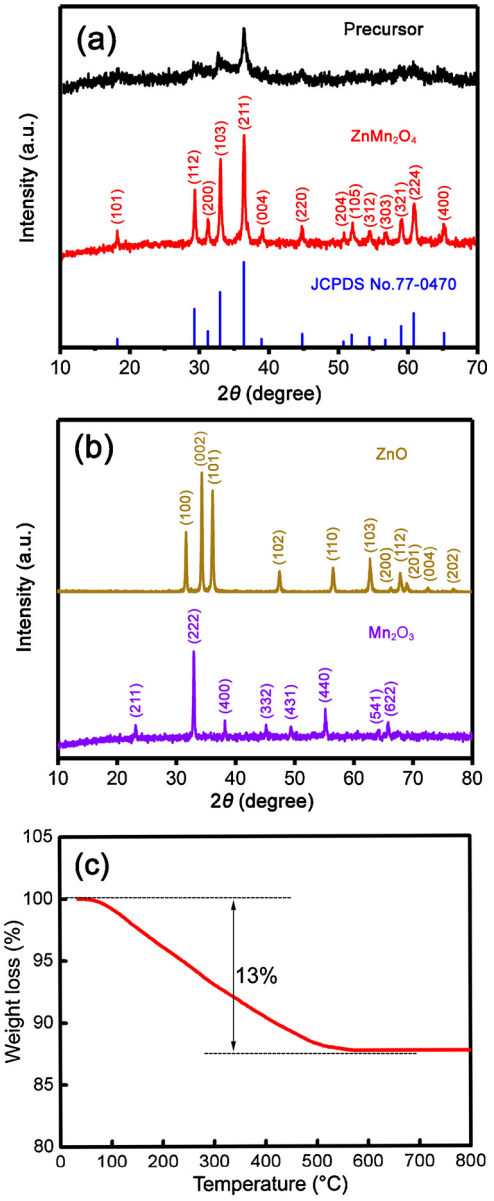

Fig. 1. (a) XRD patterns of the as-synthesized products before and after annealing; (b) XRD patterns of Zn-based oxide and Mn-based oxide after annealing; (c) TG-DTA curve of the products before annealing.

divided into two peaks, one peak at 531.6 eV and the other at 529.9 eV (Fig. 2d). The peak at 531.7 eV is ascribed to the large number of defect sites with hypoxia coordination in the nanoscale $ZnMn_2O_4$ species and the peak at 529.9 eV corresponds to a typical metal-oxygen bond [28,29]. Moreover, the calculation of peak areas in Zn 2*p* and Mn 2*p* core level spectra gives a Zn/Mn atomic ratio of about 1:2, which is similar to the design ratio of $ZnMn_2O_4$. This result is in good agreement with the XRD patterns.

The morphology and microstructural features of the metal glycolate precursor and the final product after annealing were investigated by SEM. Figs. 3a,b display the morphology of $ZnMn_2O_4$, which is similar to that of the metal glycolate precursor (Fig. S1). The $ZnMn_2O_4$ after annealing looks like nano-peanuts with diameters of 16–25 nm. The special framework can be attributed to the combustion of CTAB, which can release gases such as CO_2, H_2O and N_2 during the calcination process. CTAB is a surfactant with significant dispersibility that can enhance the system stability during the solvothermal process. If no CTAB is added into the synthetic solution, the resulting precipitate is heterogeneous and severely agglomerated, as shown in Fig. S2. Mesoporous and macroporous structure can overcome the major kinetic limitations of electrochemical processes and act as ion buffering reservoirs during the de-intercalation of lithium [29–31]. The ultra-small particles can not only provide active sites for the insertion and extraction of Li^+, but also reduce the diffusion distance of Li^+, which can overcome the diffusion limitations of LIBs [32,34]. Meanwhile, the mesoporous features have great benefits for the transport and diffusion of electrolyte during the charge-discharge process. Fig. 3d shows the elemental mapping and the EDS spectrum of the samples, indicating that the Zn, Mn, and O are uniformly distributed in $ZnMn_2O_4$. The EDS spectrum indicates that the mesoporous $ZnMn_2O_4$ nano-peanuts mainly consist of Zn, Mn and O. In addition, the atomic ratio of Zn/Mn is determined to be about 1:2, which is consistent with the stoichiometry ratio of $ZnMn_2O_4$. The same solution was established using CTAB to obtain bulk ZnO and bulk Mn_2O_3, but the products were heterogeneous, as shown in Figs. 3e and f. Under the same preparation conditions, $ZnMn_2O_4$ is much more homogeneous compared to ZnO and Mn_2O_3, which could be caused by the synergistic features of the combination of Zn ion and Mn ion.

To further investigate the microstructure of the $ZnMn_2O_4$, we also carried out extensive TEM examination of the $ZnMn_2O_4$ nano-peanuts. Figs. 4a, c show BF TEM images of $ZnMn_2O_4$. Fig. 4b presents that the as-prepared $ZnMn_2O_4$ nano-peanuts are uniform, with an average diameter of 18 nm. It can be clearly seen from Fig. 4c that the nano-peanut consists of two or three interconnected nanoparticles with a diameter of 16–25 nm, which is consistent with the SEM results. Fig. 4d shows the HRTEM image of the $ZnMn_2O_4$, which is taken along [102] zone-axis. A clear lattice fringe can be clearly seen, which corresponds to the crystal planes of $ZnMn_2O_4$ nano-peanuts. The crystal lattice spacings measured from HRTEM images are 2.86, 2.47 and 2.47 Å, respectively, which correspond to the interplanar spacings of $(0\bar{2}0)$, $(\bar{2}11)$ and $(\bar{2}\bar{1}1)$ planes of the tetragonal $ZnMn_2O_4$.

In general, both the high specific surface area and suitable pore size play important roles in the electrochemical properties of the electrode materials. Thus, an N_2 adsorption/desorption test was conducted on the activated $ZnMn_2O_4$ to evaluate the permanent porosity. As shown in Fig. 5a, the curve illustrates the reversible type-III isotherm with hysteresis loops at the relative pressure P/P_0 of 0.55–1.0, which is one of the main characteristics of mesoporous materials. The specific surface area of $ZnMn_2O_4$ is 104.16 $m^2 g^{-1}$ and the total pore volume is 0.290 cm^3 g^{-1}. The pore size distribution curve was calculated by the BJH desorption branches and the pores are in the range of 8–20 nm (Fig. 5b). The presence of a high surface area and mesoporous structure with a suitable pore size keeps the electrolyte and materials in effective contact and facilitates the diffusion of lithium ions in the electrode [35–37]. Such a mesoporous hierarchical architecture will effectively promote lithium storage, because it can enhance the diffusion of electrolyte into the active materials and buffer against the volume change during the charge-discharge process.

To study the ion diffusion process and phase transition of the electrode materials during charge-discharge process, the CV curve of $ZnMn_2O_4$ nano-peanuts was tested. Fig. 6a shows the cyclic voltammetric (CV) curves for the first six cycles of $ZnMn_2O_4$ at the potential range of 0.01–3.00 V (*vs.* Li/Li^+) with a scan rate of 0.1 mV s^{-1}. In the first cycle, there is a slight reduction peak at 1.12 V, which could be ascribed to the reduction of Mn^{3+} to Mn^{2+} [37]. Another strong reduction peak at 0.14 V is considered to be the reduction from Mn^{2+} and Zn^{2+} to metallic Mn° and Zn° in Li_2O matrix. In the meantime, it also can be connected to the formation of solid electrolyte interface (SEI) due to the electrolyte degradation, resulting in a large initial irreversible capacity [38,39]. Moreover, there is a broad and weak peak below 0.14 V, which is the formation of ZnLi alloy. The oxidation peaks at approximately 1.2 V and 1.5 V correspond to the oxidation of Mn° and Zn° to Mn^{2+} and Zn^{2+}, respectively, along with the decomposition of Li_2O matrix. In the following cycles, the oxidation peaks are similar to the first cycle, which show the analogous electrochemical process for

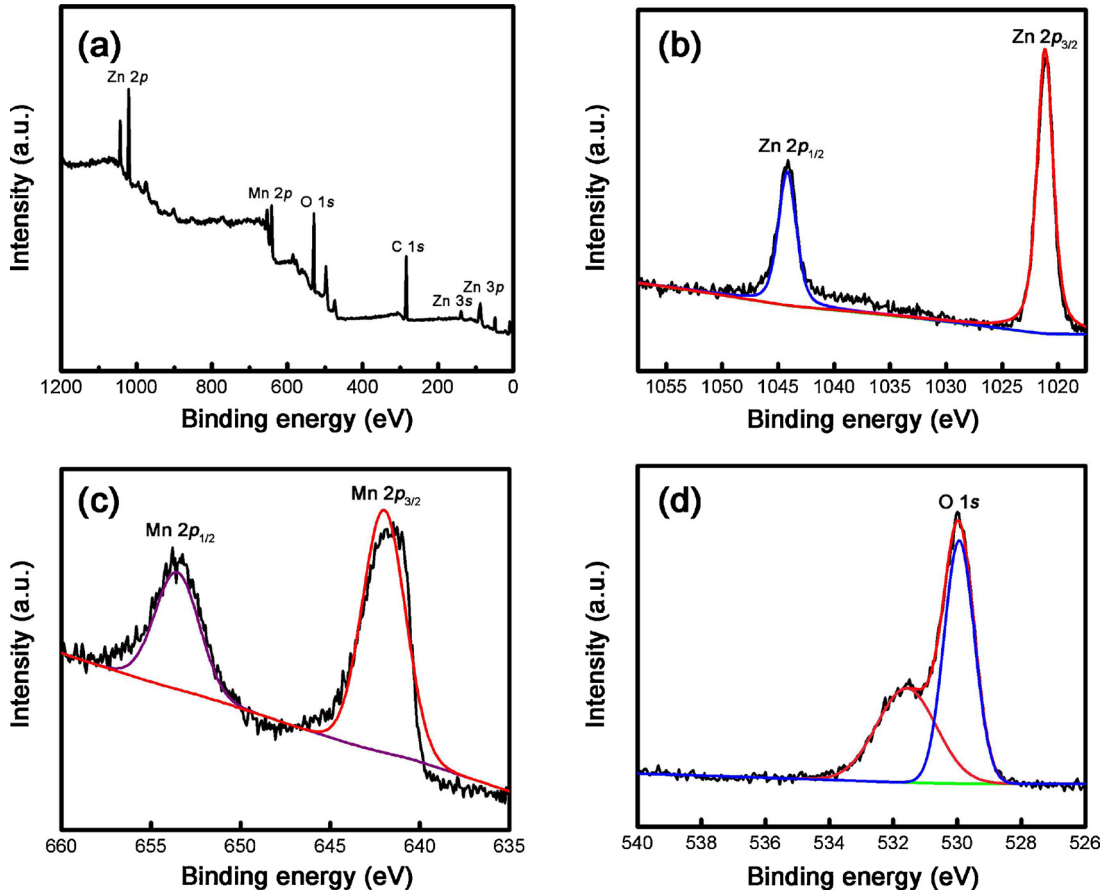

Fig. 2. XPS core level spectra of as-fabricated nanocrystalline $ZnMn_2O_4$. (a) full scan, (b) Zn 2*p*, (c) Mn 2*p*, (d) O 1*s* of $ZnMn_2O_4$.

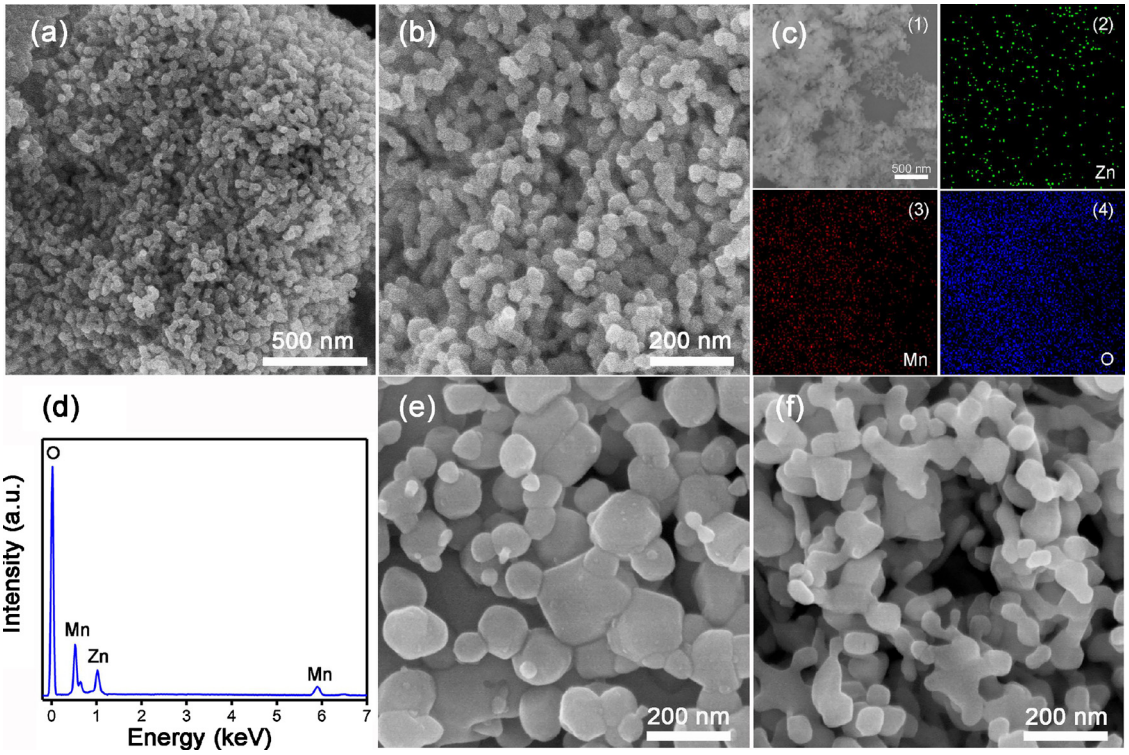

Fig. 3. (a,b) SEM images of the final $ZnMn_2O_4$; (c) A low magnification FESEM image and Zn, Mn, O elemental mapping of $ZnMn_2O_4$; (d) Typical EDS spectrum of $ZnMn_2O_4$; (e) SEM image of bulk ZnO; (f) SEM image of bulk Mn_2O_3.

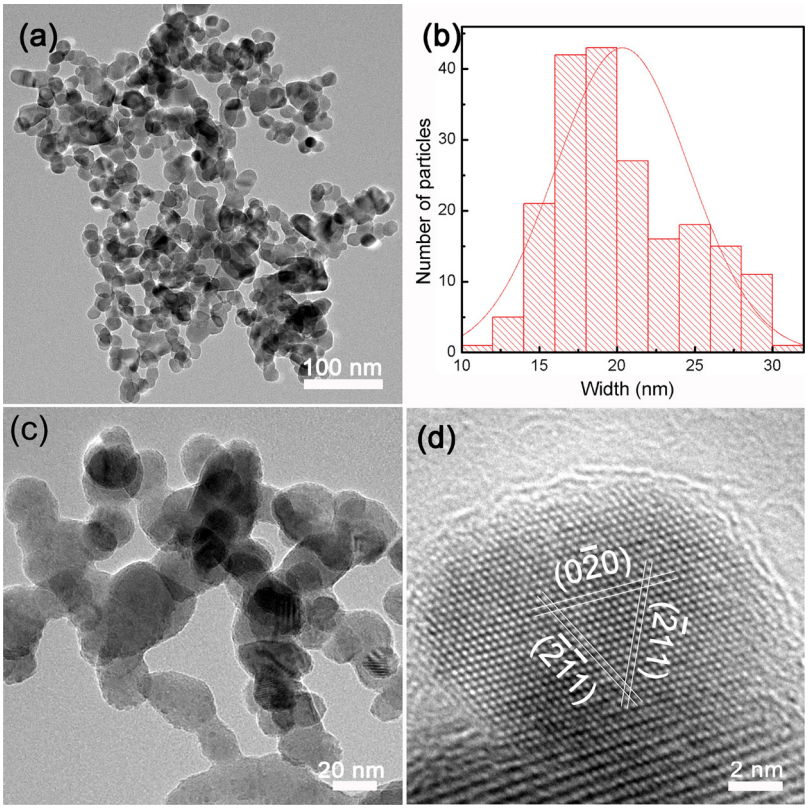

Fig. 4. (a,b) Typical BF TEM images of 3D hierarchical $ZnMn_2O_4$ nano-peanuts; (c) HRTEM image of an individual nano-peanut viewed along [102] direction; (d) Statistical size distribution of $ZnMn_2O_4$ obtained from analysis of 200 $ZnMn_2O_4$ nano-peanuts.

the anodic scan. While the reduction peaks shift from 0.14 V to 0.45 V, which may be related to the rearrangement of structure [35]. And the peaks at around 0.45/1.25 V corresponds to the redox reaction between Mn and MnO, while 0.8/1.5 V corresponds to the reduction/oxidation of ZnO [24]. The CV curves of the second and sixth cycles almost overlap, indicating high electrochemical reversibility and good structural durability of the electrode fabricated during the insertion and extraction of Li^+ from the $ZnMn_2O_4$ nano-peanuts [27].

Fig. 6b shows the representative galvanostatic discharge-charge curves of the $ZnMn_2O_4$ nano-peanuts electrode from the first to third cycles, which was tested at a current density of 100 mA g^{-1} (*vs.* Li/Li^+). Obviously, the initial discharge process can be divided into three stages. In the first stage, the voltage drops very quickly. In the second stage, the curve exhibits a short platform at about 1.25 V, which is assigned to the Mn-III/II reduction, and also shows a long platform at about 0.45 V, which corresponds to the formation of Zn°, Mn° and Li-Zn alloy, consistent with the CV results. In the third stage, the voltage slowly drops and this process stores most of the lithium ions and contributes to the most of discharge capacity. The initial discharge and charge capacities of the $ZnMn_2O_4$ nano-peanuts are 1289 and 863 mA h g^{-1}, respectively, and the initial charge-discharge coulombic efficiency is 64.5%. This may be ascribed to the formation of the SEI layer and electrolyte decomposition, which is common to most anode materials [32]. In the second cycle, the discharge profile exhibits a specific capacity of approximately 870 $mAhg^{-1}$, which is similar to the first charge curve, but with a lower capacity and a higher plateau voltage. Moreover, the subsequent discharge-charge curves demonstrate a qualitative resemblance to the second cycle curve, except for a slight decreasing capacity and a stable capacity. All of these phase transitions after the reduction and oxidation processes are in good agreement with the CV results.

As presented in Fig. 6d, the rate performance of $ZnMn_2O_4$ nano-

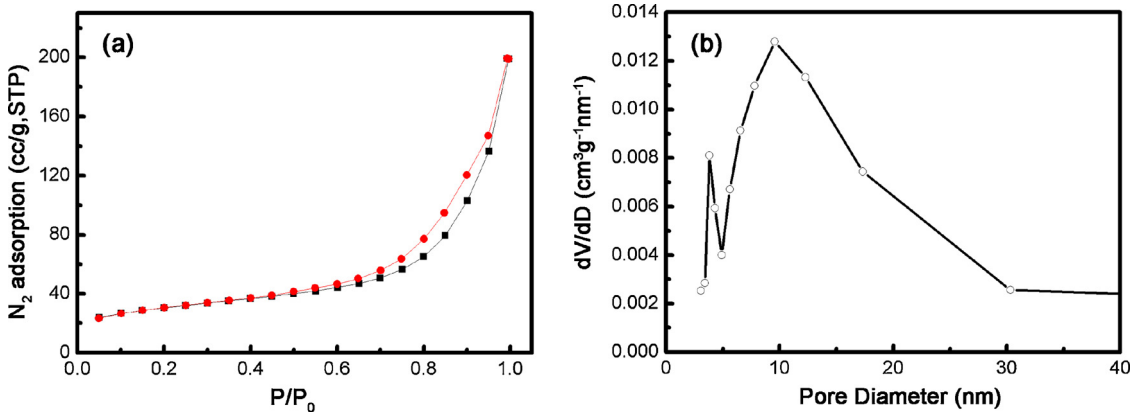

Fig. 5. (a) N_2 adsorption-desorption isotherms of $ZnMn_2O_4$; (b) pore size distribution curve of $ZnMn_2O_4$.

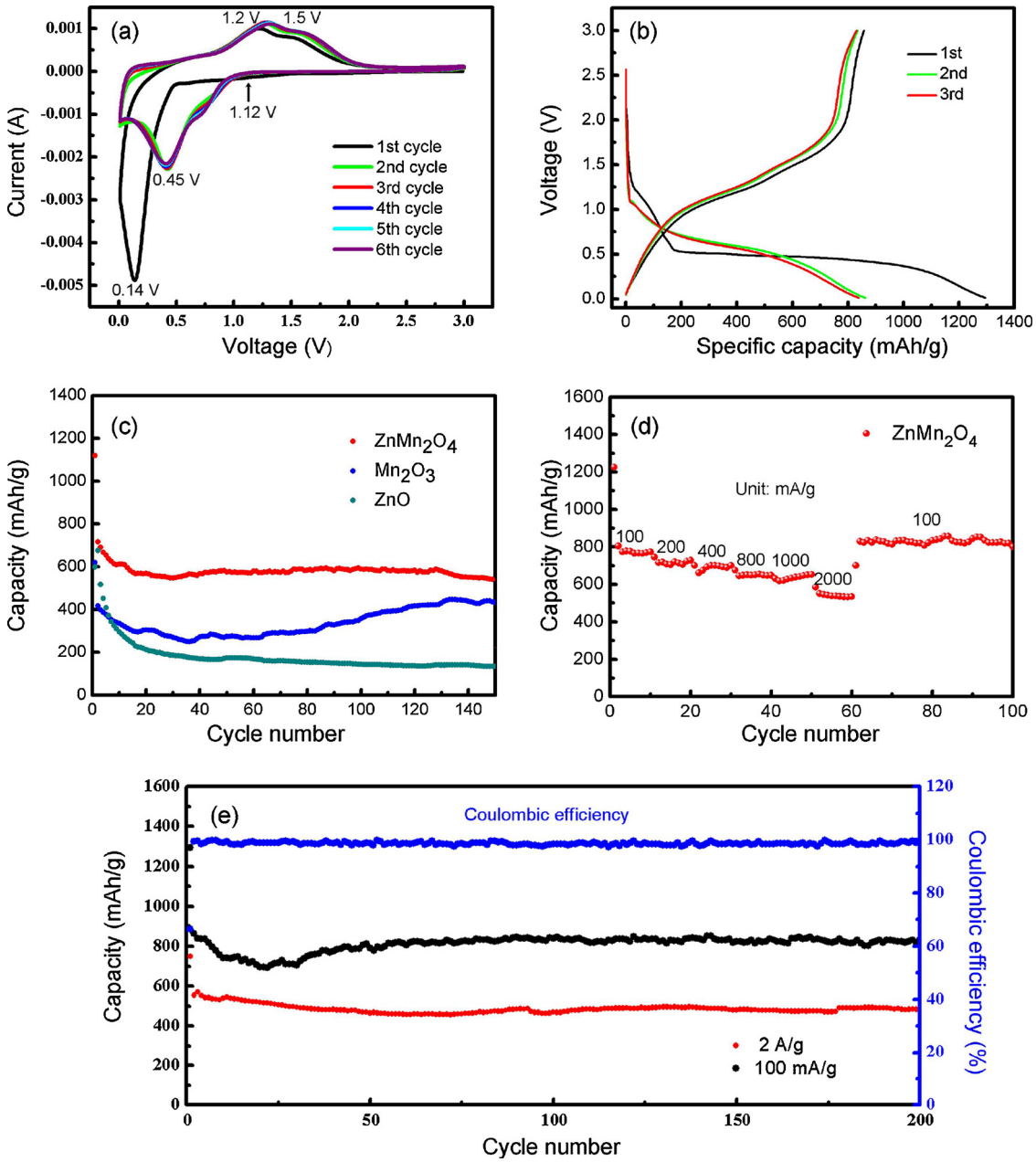

Fig. 6. (a) Cyclic voltammetry curves of $ZnMn_2O_4$ nano-peanuts at 0.1 mV s^{-1}; (b) Initial voltage vs. capacity curves of the $ZnMn_2O_4$ nano-peanuts at 100 mA g^{-1}; (c) Cycle performance of $ZnMn_2O_4$, ZnO and Mn_2O_3 at the same current density, 500 mA g^{-1}; (d) Rate performance of $ZnMn_2O_4$ nano-peanuts at various current densities; (e) Cycle performance of $ZnMn_2O_4$ at 100 mA g^{-1} and 2 A g^{-1}.

peanuts was measured at various current densities from 0.1 to 2 A g^{-1}. Obviously, the capacities of $ZnMn_2O_4$ decrease as the currents increase. When the current rises to 2 A g^{-1}, the capacity is 550 mA g^{-1}. More importantly, when the current density is restored to 0.1 A g^{-1}, the capacity is higher than the initial capacity at 0.1 A g^{-1}. The cycling performance of the $ZnMn_2O_4$ was tested *via* the galvanostatic charge-discharge cycling at a current density of 100 mA g^{-1} (Fig. 6e). The capacity curve for 100 mA g^{-1} showed a reduction in the first few cycles, which may be due to the irreversible reactions and rapid structure changes. Afterwards, the capacity curves decreased slightly and then stabilized at 812 mA h g^{-1} after 200 cycles. Such a phenomenon was generally observed for the transition metal oxide-based anodes and was commonly ascribed to the reversible formation of a polymeric gel-like film that originates from kinetic activation in the electrode [11,26]. To further evaluate the electrochemical properties of the $ZnMn_2O_4$ nano-peanuts, the battery was charged and discharged at a high current density of 2 A g^{-1}. To our surprise, 516 mA h g^{-1} discharge capacity remained after 200 cycles. As shown in Fig. 6c, we make the comparative cycling performance of $ZnMn_2O_4$ nano-peanuts, bulk ZnO and bulk Mn_2O_3 at a current density of 500 mA g^{-1}. It can be seen that the $ZnMn_2O_4$ nano-peanuts can maintain a reversible capacity value of 586 mA h g^{-1} after 30th cycles. Subsequently, the reversible capacity increased slightly and then stabilized. The bulk Mn_2O_3 begins to rise at about the 40th cycle, but starts to decline after the 150th cycle. The reversible capacity of the bulk ZnO is the worst among the three materials. The above results indicate that the nano-peanuts-like $ZnMn_2O_4$ possesses excellent electrochemical properties. As an anode material, the electrochemical performance of $ZnMn_2O_4$ nanostructures could be comparable to outstanding performance of magnesium molybdate in the battery system [33]. All in all, the excellent stability of $ZnMn_2O_4$

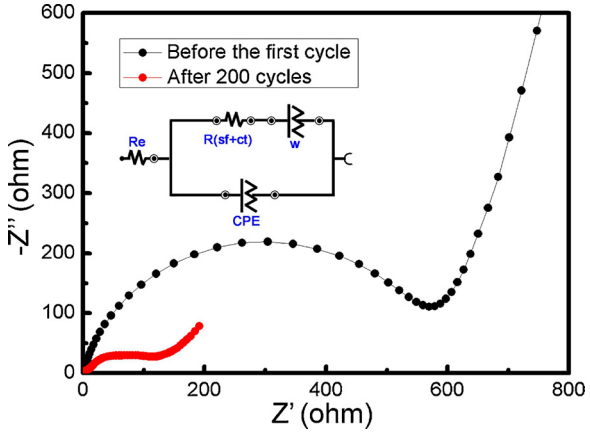

Fig. 7. EIS of $ZnMn_2O_4$ nano-peanuts before the first cycle and at after the 200th cycle. Inset is the equivalent electrical circuit.

can be attributed to the homogeneous nanoparticles and the heterogeneous pores distributed among the particles [6,7,28].

To further explore excellent electrochemical performance of the interconnected mesoporous $ZnMn_2O_4$ nano-peanuts, the EIS measurements were performed. As shown in Fig. 7, typical EIS data of the bare charged electrodes during the first and the 200th cycle are represented in Nyquist plots (Z' vs. -Z''). In the medium frequency range, the diameter of the semicircle indicates the Li^+ transport resistance of the SEI layer (R_{sf}) and the charge-transfer resistance (R_{ct}) [20]. According to the fitting values of the equivalent circuit, the $R_{(sf+ct)}$ of the first cycle is 565 Ω, and it drops to 99.4 Ω after 200 cycles. Obviously, the semicircle diameter of the electrodes (Ω) after cycling is much smaller than the electrode (Ω) before cycling in the high-medium frequency regions, which implies that the electrodes after cycling possess a more efficient charge transfer than those before cycling, thus suggesting that the $ZnMn_2O_4$ nano-peanuts with interconnected mesoporous structure can reduce the resistance and facilitate the electron transport during charge and discharging processes.

The XPS measurement was carried out to examine the elemental oxidation state and composition of the $ZnMn_2O_4$ samples after 200 cycles. Fig. 8a shows the XPS spectrum of Zn 2*p*, in which two typical peaks located at 1022.1 and 1045.1 eV proved to be Zn $2p_{3/2}$ and Zn $2p_{1/2}$. The energy difference between Zn $2p_{1/2}$ and Zn $2p_{3/2}$ is approximately 23 eV, which is well in the accordance with Zn^{2+} according to previous reports. It can be confirmed that ZnO exists after cycling [6,11,20]. As shown in Fig. 8b, the peaks at 642.1 eV and 653.6 eV are Mn $2p_{3/2}$ and Mn $2p_{1/2}$ with a satellite peak at 647.8 eV, which is the characteristic peak of Mn^{2+}, thus MnO is also present in the compounds after the cycling [6,11]. Because of the existence of ZnO and MnO after cycling, the discharge capacity increases slightly and is higher than the theoretical capacity of $ZnMn_2O_4$.

To elucidate the structural stability of $ZnMn_2O_4$ nano-peanuts, a detailed microstructure analysis of the electrode materials (after the 200th cycle at a current rate of 100 mA g^{-1}) was performed. The additional features in the TEM image (Fig. 9a) could be sodium alginate (SA) and carbon black, which were introduced during the preparation process of the working electrode. The electrode materials might have slight volume expansion after cycling, but will not coalesce or rupture after cycling. Thus, the morphology is basically consistent with that before cycling. It suggests that the mesoporous interconnected 3D framework can prevent the structure from crushing and keep the $ZnMn_2O_4$ stable, thus improving the cycling performance of LIBs. Figs. 9b, c show typical HRTEM images of a single particle, and the lattice spacing is measured to be 2.61 Å, corresponding to interplanar spacing of (002) plane of ZnO (Fig. 9b). The crystal lattice spacing is measured to be 2.56 Å, which is consistent with the interplanar spacing of (111) plane of MnO (Fig. 9c). Figs. 9b, c indicate the reversibility of the conversion reaction of $ZnMn_2O_4$. Both XPS and TEM results all demonstrate the presence of ZnO and MnO in the compounds after cycling, which corresponds to the CV plot in Fig. 6a.

4. Conclusions

In summary, the $ZnMn_2O_4$ nano-peanuts with interconnected mesoporous structure were successfully synthesized by a facile one-step solvothermal method. The method is simple, no-toxic and environment-friendly. The interconnected mesoporous structure integrates three advantages: special mesoporous structure, a high specific surface and interconnected walls, which shorten the Li ion pathway, reduce the resistance, buffer the volume change and accommodate or alleviate strain alleviate during the charge-discharge process. As anode materials for LIBs, the interconnected mesoporous $ZnMn_2O_4$ nano-peanuts have excellent cycling performance, high reversible capacity and good rate capability. The XPS and TEM results of the electrode materials after cycling show that the original appearance can be preserved and that ZnO and MnO are generated, thereby, the discharge capacity increases slightly and is stable, also is higher than the theoretical capacity of $ZnMn_2O_4$. The interconnected mesoporous $ZnMn_2O_4$ nano-peanuts are expected to extend for synthesis of other MTMOs with enhanced energy storage applications.

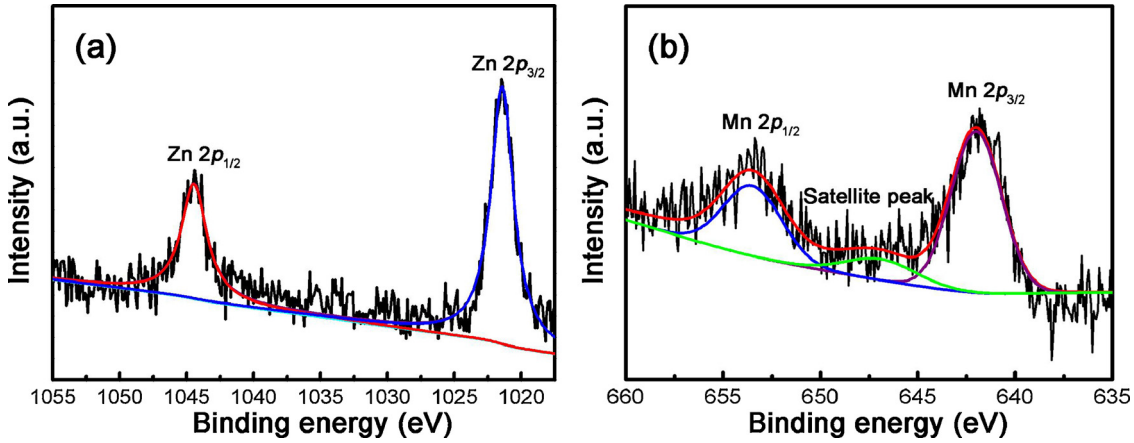

Fig. 8. XPS spectra of the material after the 200 cycles. (a) Zn 2*p*, (b) Mn 2*p*.

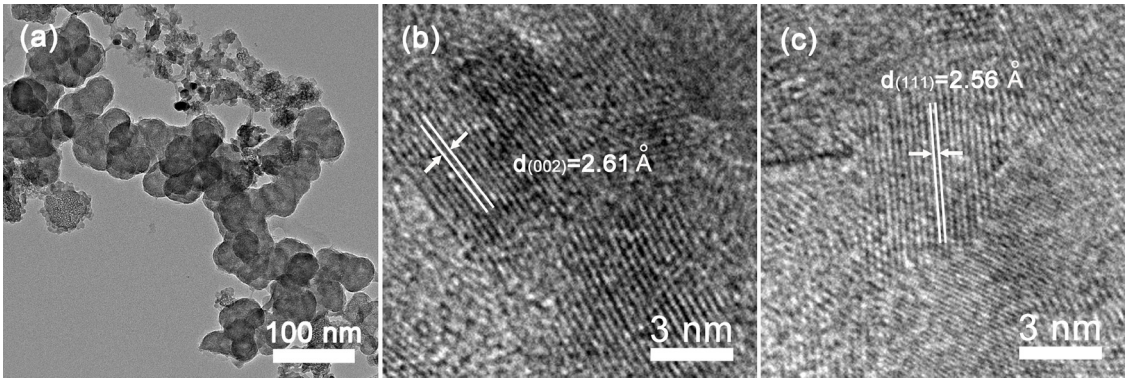

Fig. 9. (a) Typical TEM image of $ZnMn_2O_4$ nano-peanuts electrode after the 200th cycle at 100 mA g^{-1}; (b,c) Typical HRTEM images of $ZnMn_2O_4$ nano-peanuts electrode at state of charging to 3.0 V after the 200th cycle at 100 mA g^{-1}.

Acknowledgments

We would like to thank the financial support from the National Natural Science Foundation of China (Grant No.: 10974105, 21701095), Natural Science Foundation of Shandong Province, China (Grant No.: ZR2017BEM007), China Postdoctoral Science Foundation (2017M622131), Program of Science and Technology for Higher Education in Shandong Province, China (Grant No.: J17KA010), the Recruitment Program of High-end Foreign Experts (Grant Nos.: GDW20163500110 and GDW20173500154). Y. Q. Wang would also like to thank the financial support from the Top-notch Innovative Talent Program of Qingdao City (Grant No.: 13-CX-08), the Taishan Scholar Program of Shandong Province, and Qingdao International Center for Semiconductor Photoelectric Nanomaterials and Shandong Provincial University Key Laboratory of Optoelectrical Material Physics and Devices.

References

[1] J.–M. Tarascon, M. Armand, Issues and challenges facing rechargeable lithium batteries, Nature 414 (2001) 359–367.
[2] J.B. Goodenough, Y. Kim, Challenges for rechargeable Li batteries, Chem. Mater. 22 (2010) 587–603.
[3] M.V. Reddy, G.V. Subba Rao, B.V.R. Chowdari, Metal oxides and oxysalts as anode materials for Li ion batteries, Chem. Rev. 113 (2013) 5364–5457.
[4] B. Liu, X.Y. Zhao, Y. Tian, D. Zhao, C.W. Hu, M.H. Cao, A simple reduction process to synthesize MoO_2/C composites with cage-like structure for high-performance lithium-ion batteries, Phys. Chem. Chem. Phys. 15 (2013) 8831–8837.
[5] Z.F. Ma, T.B. Zhao, Reduced graphene oxide anchored with MoO_2 nanorods as anode for high rate and long cycle lithium ion batteries, Electrochim. Acta 201 (2016) 165–171.
[6] J.W. Chen, X. Wang, J.X. Wang, P.S. Lee, Sulfidation of NiMn-layered double hydroxides/graphene oxide composites toward supercapacitor electrodes with enhanced performance, Adv. Energy Mater. 6 (2016) 1501745.
[7] V. Aravindan, Y.-S. Lee, S. Madhavi, Research progress on negative electrodes for practical Li-ion batteries: beyond carbonaceous anodes, Adv. Energy Mater. 5 (2015) 1402225.
[8] B.C. Sekhar, P. Packiyalakshmi, N. Kalaiselvi, Synergistic effect of flakes containing interconnected nanoparticles and conducting graphene additive to qualify $ZnMn_2O_4$ as potential lithium battery anode, ChemElectroChem 4 (2016) 1154–1164.
[9] S.Q. Zhu, Y.Y. Shi, Q.L. Chen, Z.Y. Chen, R.Q. Bao, C. Yang, L.R. Hou, G. Pang, C.Z. Yuan, Self-sacrificial template formation of ultrathin single-crystalline $ZnMn_2O_4$ nanoplates with enhanced Li-storage behaviors for Li-ion batteries, RSC Adv. 6 (2016) 2024–2027.
[10] Q. Sun, M. Bijelic, A.B. Djurisic, C. Suchomski, X. Liu, M.H. Xie, A.M.C. Ng, H.K. Li, K. Shih, S.J. Burazer, Z. Skoko, I. Djerdj, J. Popovic, Graphene oxide wrapped $ZnMn_2O_4$ as high performance lithium ion battery anode, Nanotechnology 28 (2017) 455401.
[11] T. Zhang, H. Liang, C.D. Xie, H.L. Qiu, Z.B. Fang, L. Wei, H.J. Yue, G. Chen, Y.J. Wei, C.Z. Wang, D. Zhao, Morphology-controllable synthesis of spinel zinc manganate with highly reversible capability for lithium ion battery, Chem. Eng. J. 326 (2017) 820–830.
[12] Z.Y. Wang, L. Zhou, X.W. Lou, Metal oxide hollow nanostructures for lithium-ion batteries, Adv. Mater. 24 (2012) 1903–1911.
[13] S.-W. Kim, H.-W. Lee, P. Muralidharan, D.-H. Seo, W.-S. Yoon, D.K. Kim, K. Kang, Electrochemical performance and *ex situ* analysis of $ZnMn_2O_4$ nanowires as anode materials for lithium rechargeable batteries, Nano Res. 4 (2011) 505–510.
[14] Y. Tian, Z.X. Chen, W.J. Tang, Z.H. Yang, W.X. Zhang, S. Li, K. Wang, Y.H. Sun, Q. Xin, B. Guo, A facile synthetic protocol to construct 1D Zn-Mn-Oxide nanostructures with tunable compositions for high-performance lithium storage, J. Alloy. Compd. 720 (2017) 376–382.
[15] Y. Xiao, C.W. Hu, M.H. Cao, High lithium storage capacity and rate capacity achieved by mesoporous Co_3O_4 hierarchical nanobundles, J. Power Sources 247 (2014) 49–56.
[16] G.Q. Zhang, L. Hu, H.B. Wu, H.E. Hoster, X.W. Lou, Formation of $ZnMn_2O_4$ ball-in-ball hollow microspheres as a high-performance anode for lithium-ion batteries, Adv. Mater. 24 (2012) 4609–4613.
[17] L.F. Shen, Q. Che, H.S. Li, X.G. Zhang, Mesoporous $NiCo_2O_4$ nanowire arrays grown on carbon textiles as binder-free flexible electrodes for energy storage, Adv. Funct. Mater. 24 (2014) 2630–2637.
[18] F.M. Courtel, Y.A. Lebdeh, I.J. Davidson, $ZnMn_2O_4$ nanoparticles synthesized by a hydrothermal menthod as an anode material for Li-ion batteries, Electrochim. Acta 71 (2012) 123–127.
[19] F.M. Courtel, H. Duncan, Y.A. Lebdeh, I.J. Davidson, High capacity anode materials for Li-ion batteries based on spinel metal oxides AMn_2O_4 (A = Co, Ni, and Zn), J. Mater. Chem. 11 (2011) 10206–10218.
[20] Z.C. Bai, N. Fan, C.H. Sun, Z.C. Ju, C.L. Guo, J. Yang, Y.T. Qian, Facile synthesis of loaf-like $ZnMn_2O_4$ nanorods and their excellent performance in Li-ion battery, Nanoscale 5 (2013) 2442–2447.
[21] J. Zhao, F.Q. Wang, P.P. Su, M.R. Li, J. Chen, Q.H. Yang, C. Li, Spinel $ZnMn_2O_4$ nanoplate assemblies fabricated via “escape-by-crafty-scheme” strategy, J. Mater. Chem. 22 (2012) 13328–13333.
[22] L. Zhao, H.B. Wu, T. Zhu, X.W. Lou, Facile preparation of $ZnMn_2O_4$ hollow microspheres as high-capacity anode for lithium-ion batteries, J. Mater. Chem. 22 (2012) 827–829.
[23] L.W. Yin, Zh.W. Zhang, Zh.Q. Li, F.B. Hao, Q. Li, C.H.X. Wang, R.H. Fan, Y.X. Qi, Spinel $ZnMn_2O_4$ nanocrystal-anchored 3D hierarchical carbon aerogel hybrids as anode materials for lithium ion batteries, Adv. Funct. Mater. 24 (2014) 4176–4185.
[24] T. Zhang, H.J. Yue, H.L. Qiu, Y.J. Wei, C.Z. Wang, G. Chen, D. Zhang, Nano-particle assembled porous core-shell $ZnMn_2O_4$ microspheres with superb performance for lithium batteries, Nanotechnology 28 (2017) 105403.
[25] J.G. Kim, S.H. Lee, Y. Kim, W.B. Kim, Fabrication of free-standing $ZnMn_2O_4$ mesoscale tubular arrays for lithium-ion anode with highly reversible lithium storage properties, ACS Appl. Mater. Interface 5 (2013) 11321–11328.
[26] M.M. Sundaram, A. Biswal, D. Mitchell, R. Jones, C. Fernandez, Correlation among physical and electrochemical behaviour of nanostructured electrolytic manganese dioxide from leach liquor and synthetic for aqueous asymmetric capacitor, Phys. Chem. Chem. Phys. 18 (2016) 4711–4720.
[27] L.H. Zhang, S.Q. Zhu, H. Gao, L.R. Hou, C.Z. Yuan, Hierarchical porous $ZnMn_2O_4$ hollow nanotubes with enhanced lithium storage toward lithium-ion batteries, Chem. Eur. J. 21 (2015) 10771–10777.
[28] C.Z. Yuan, L.H. Zhang, L.R. Hou, L. Zhou, G. Pang, L. Lian, Scalable room-temperature synthesis of mesoporous nanocrystalline $ZnMn_2O_4$ with enhanced lithium storage properties for lithium-ion batteries, Chem. Eur. J. 21 (2015) 1262–1268.
[29] S.H. Li, J.W. Chen, M.Q. Cui, G.F. Cai, J.X. Wang, P. Cui, X.F. Gong, P.S. Lee, A high-performance lithium-ion capacitor based on 2D nanosheet materials, Small 13 (2017) 1602893.
[30] H.L. Wang, Z.W. Xu, Z. Li, K. Cui, J. Ding, A. Kohandehghan, X.H. Tan, B. Zahiri, B.C. Olsen, C.M.B. Holt, D. Mitlin, Hybird device employing three-dimensional arrays of MnO in carbon nanosheets bridges battery-supercapacitor divide, Nano Lett. 14 (2014) 1987–1994.
[31] T.Z. Yuan, Y.Z. Jiang, W.P. Sun, B. Xiang, Y. Li, M. Yan, B. Xu, S.X. Dou, Ever-increasing pseudocapacitance in RGO-MnO-RGO sandwich nanostructures for ultahigh-rate lithium storage, Adv. Funct. Mater. 26 (2016) 2198–2206.
[32] X.Y. Zhao, M.H. Cao, B. Liu, Y. Tian, C.W. Hu, Interconnected core-shell MoO_2 microcapsules with nanorod-assembled shells as high-performance lithium-ion battery anodes, J. Mater. Chem. 22 (2012) 13334–13340.
[33] M. Minakshi, D.R.G. Mitchell, A.R. Munnangi, A.J. Barlow, M. Fichtner, New insight into the electrochemistry of magnesium molybdate hierarchical architectures for high performance sodium devices, Nanoscale 10 (2018) 13277–13288.

[34] N.N. Wang, X.J. Ma, H.Y. Xu, L. Chen, J. Yue, F.E. Niu, J. Yang, Y.T. Qian, Porous $ZnMn_2O_4$ microspheres as a promising anode material for advanced lithium-ion batteries, Nano Energy 6 (2014) 193–199.
[35] Y. Luo, D.D. Yuan, M.S. Balogun, H. Yang, W.T. Qiu, J.C. Liu, P. Liu, Y.X. Tong, Dual doping strategy enhanced the lithium storage properties of graphene oxide binary composites, J. Mater. Chem. A Mater. Energy Sustain. 4 (2016) 13431–13436.
[36] V. Etacheri, Gulaim A. Seisenbaeva, J. Caruthers, G. Daniel, J.-M. Nedelec, Vadim G. Kessler, Vilas G. Pol, Ordered network of interconnected SnO_2 nanoparticles for excellent lithium-ion storage, Adv. Energy Mater. 5 (2015) 1401289.
[37] T. Zhang, H.L. Qiu, M. Zhang, Z.B. Zhang, X.S. Zhao, L. Wang, G. Chen, Y.J. Wei, H.J. Yue, C.Z. Wang, D. Zhang, A unqiue 2D-on-3D architecture developed from $ZnMn_2O_4$ and CMK-3 with excellent performance for lithium ion batteries, Carbon 123 (2017) 717–725.
[38] P. Li, J.Y. Liu, Y. Liu, Y.W. Wang, Z.T. Li, W.T. Wu, Y. Wang, L.H. Yin, H. Xie, M.B. Wu, X.J. He, J.S. Qiu, Three-dimensional $ZnMn_2O_4$/porous carbon framework from petroleum asphalt for high performance lithium-ion battery, Electrochim. Acta 180 (2015) 164–172.
[39] X.Q. Chen, Y.M. Zhang, H.B. Lin, P. Xia, X. Cai, X.G. Li, X.P. Li, W.S. Li, Porous $ZnMn_2O_4$ nanospheres: facile synthesis through microemulsion method and excellent performance as anode of lithium ion battery, J. Power Sources 312 (2016) 137–145.